Improvements in the numerical prediction of fully-suspended slurry flow in horizontal pipes

Gianandrea Vittorio Messa *, Stefano Malavasi

DICA, Politecnico di Milano, Piazza Leonardo da Vinci, 32, 20133 Milano, Italy

Received 25 August 2014
Received in revised form 15 October 2014
Accepted 17 October 2014
Available online 31 October 2014

1. Introduction

Pipe flows of solid–liquid mixtures in the form of slurry are commonly encountered in many applications. A significant example is the slurry pipelines used to transport mineral concentrate from a miner-al processing plant near a mine. The pressure gradient is perhaps the most relevant parameter to engineers and designers, as it dictates the selection of pump capacity.

Doron and Barnea [1] identified the flow patterns of slurries flowing in horizontal pipes as the flow rate decreases: (a) fully-suspended flow, in which all the particles are suspended; (b) flow with a bed (moving/stationary), in which the particles accumulate at the pipe bottom and form a bed either sliding or fixed. The transition between fully-suspended and bed flows corresponds to a minimum in the plot of pressure gradient, $\Delta P/\Delta z$, versus slurry superficial velocity, V_s, which is the ratio of the slurry volumetric flow rate and the area of the pipe section (Fig. 1). The value of superficial velocity at which the transition occurs is referred to as deposition velocity, V_D, and can be estimated by many empirical formulas including the one proposed by Wasp [2], as follows:

$$V_{D,\mathrm{Wasp}} = 4\left(\frac{d_p}{D_p}\right)^{1/6} C^{1/5}\sqrt{2|\mathbf{g}|\left(\frac{\rho_p}{\rho_f}-1\right)} \tag{1}$$

where d_p is the particle size, D_p is the pipe diameter, C is the delivered solid volume fraction, $\mathbf{g}$ is the gravity acceleration vector, and ρ_p and ρ_f are the densities of the particles and the fluid, respectively. By comparison against a large dataset of experimental measurements available in the literature, Messa [3] evidenced that Eq. 1 is likely to underesti-mate the deposition velocity.

In bed flows Coulombic stresses occur among the particles in permanent contact with each other. These stresses are transferred to the pipe wall and produce a solid shear stress which contributes to friction if the layer of particles is not stationary. However, a slurry pipeline is usually run at somewhat higher velocity compared to V_D [4], and therefore being able to correctly predict the behavior of fully-suspended flows is of considerable importance from an engineering point of view. In the present work we will focus on the fully-suspended flow regime. Therefore, we will refer only to the right part of the plot of Fig. 1.

In fully-suspended flows the interactions among the particles are in the form of occasional collisions rather than permanent contacts. The interactions among fluid, particles, and the pipe wall determine the dissipation occurring during the transport of the slurry. It is a well established practice to attribute the pressure gradient of the fully-suspended solid–liquid slurry to two different frictional mechanisms, referred to as viscous “liquid-like” friction and mechanical friction [5]. The former is due to the slurry viscosity in the laminar sublayer, while the latter is due to the impingements of the traveling suspended particles with the pipe wall. These mechanisms are strictly dependent upon the relationship between the particle size and the boundary layer

---

* Corresponding author. Tel.: +39 02 2399 6287.
E-mail address: gianandreavittorio.messa@polimi.it (G.V. Messa).

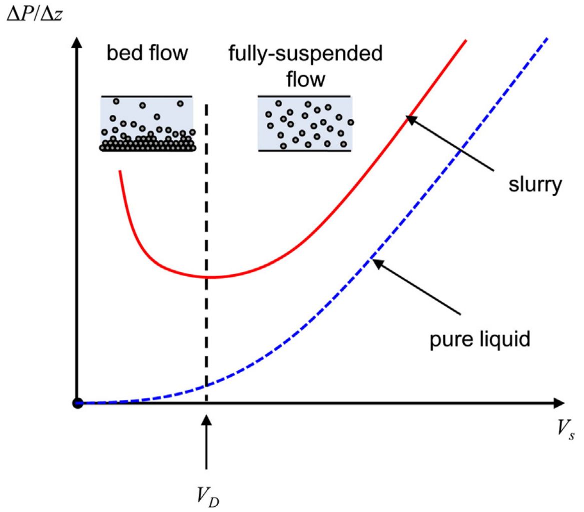

Fig. 1. Qualitative plot of pressure gradient, $\Delta P/\Delta z$, versus slurry superficial velocity, V_s. Identification of the flow regimes and comparison against the single-phase case.

characteristics which, in some previous researches [6-8], was quantified by means of a dimensionless particle size:

$$d_p^+ = \frac{\rho_f d_p u_f^*}{\mu_f} \tag{2}$$

where u_f^* is the friction velocity of the fluid, namely the square root of the ratio between the fluid wall shear stress $\tau_{w,f}$ and the fluid density ρ_f, and μ_f is the dynamic viscosity of the fluid.

If the particles are small enough to be trapped within the viscous sublayer (say for $d_p^+ \ll 5$), they increase the density and the viscosity of the carrying fluid. This determines an increase of the viscous "liquid-like" friction which, in turn, results in higher pressure gradient compared to the single-phase case. Conversely, the mechanical contact friction does not play a role unless the concentration of solids near the wall becomes very high. As a consequence of the above, under these conditions the pressure gradient can be estimated using an "equivalent-fluid" model in which the slurry is interpreted as a single-phase fluid with increased density and viscosity.

Slurries with particles which are larger compared to the thickness of the viscous sublayer, which are the topic of this paper, exhibit a completely different behavior. In this case, the particles do not affect the fluid dynamic properties of the carrying fluid in the viscous sublayer, and the impingements between the particles and the pipe wall become significant. The impingements are a result of the dispersive action of both turbulence and particle collisions, and generate a solid dispersive wall shear stress $\tau_{w,p}$ which acts in conjunction with the liquid-like friction.

Due to the considerable interest that slurry flows arouse, especially in the field of mining industry, several models have been developed for the estimation of $\tau_{w,p}$ starting from bulk parameters like the slurry superficial velocity V_s, the pipe diameter D_p, and the characteristics of the mixture. These models are usually derived from a generalization of the original equation for Bagnold's stress in the inertial regime of the sheared annular flows and calibrated by using pressure-drop data. The following correlation, proposed by Ferre and Shook [9], includes the key functional dependencies:

$$\frac{\tau_{w,p}}{\rho_s V_s^2} = 0.0214 Re_s^{-0.36} \left(\frac{d_p}{D_p}\right)^{0.99^{1.31}} \tag{3}$$

where Re_s is defined as $\rho_s V_s d_p/\mu_f$ and λ is the linear volume fraction:

$$= \left[\left(\frac{\alpha_{\max}}{C}\right)^{1/3} - 1\right]^{-1} \tag{4}$$

in which $\alpha_{\max}$ is the maximum packing volume fraction. A similar expression, accounting for the dependence upon λ only, was proposed by Gillies and Shook [10] some years later. Other and more recent corre-lations are those of Matousek [11], Gillies et al. [7], and Bartosik [12]. It is worth noticing that the above mentioned formulas for $\tau_{w,p}$ have been developed to be employed as part of physically-based models based on a global formulation for the estimation of the pressure gradient.

Moreover, anomalous pressure gradients and volume fraction distri-butions have been observed in some experiments [13-16]. In order to explain these findings, some authors argued for the existence of a hy-drodynamic lift force repelling particles from the walls, which is effec-tive only when the center of the particles lies in a certain band of distances from the wall. Actually, the origin of this force, which increases with the delivered solid volume fraction, is still rather obscure. Wilson and Sellgren [17] attribute it to the interaction between a solid particle and liquid flow of the steep velocity gradient, which causes its rotation and develops a pressure differential over the particles. They developed a model for this force, later revised by Wilson et al. [8], and reported that, for sand–water slurries, the hydrodynamic lift force is not effective for particles smaller than about 150 μm and larger than about 400 μm. The effect of the hydrodynamic lift force was also observed in slurries made of water and glass beads of 440 μm size [15].

The use of CFD techniques for the simulation of solid–liquid slurry flows is gaining ground in recent years, not only because of the greater information about the structure of the flow that can be gathered, but also because of the versatility of this approach, which virtually allows simulating whatever kind of system at whatever scale. The Eulerian–Eulerian models, referred to as "two-fluid" models, are the only ones which allow simulating dense flows with acceptable computational cost. These models interpret both phases as interpenetrating continua and solve for their average flow properties. The two-fluid model that we proposed in a previous work [6] showed comparable or better agree-ment with the experimental evidence than similar models [18-21], and it also overcame the main limitations inferred from inspection of these earlier papers, namely susceptibility to numerical instability and high computational cost. In particular, it was capable in predicting the pres-sure gradient data of different experimenters [7,22,23] within about ± 20% of the measured values (Fig. 2). In a later stage of our research, this two-fluid model was successfully applied to more complex geome-tries, such as sudden expansions [24], pipe bends [25], and choke valves [26].

Nevertheless, further research had to be carried out regarding certain aspects – common to all two-fluid models and not exclusive to ours – of modeling rather than numerical nature. For example, none of the existing models takes explicitly into account the effect of particle shape, which proved to affect significantly the behavior of the slurry [22]. Moreover, the wall boundary condition for the solid phase, which is a key parameter for correctly predicting the pressure gradient, is not well established. This is one of the most restricting uncertainties in the use of the two-fluid models in multiphase simulations [27,28]. In slurry pipe flow computations different options have been considered. Ekambara et al. [19] set the velocity of the particles to zero at the pipe wall, but only briefly explored the capacity of their model to reproduce the pressure gradient. Kaushal et al. [21] applied the standard wall func-tion of Launder and Spalding [29] for single-phase flows to both phases when modeling the pipeline flow of fine particles at high concentration, without reporting the equations actually solved. Chen et al. [18] employed the wall boundary conditions developed by Johnson and Jackson [30] for predicting the flow properties of slurries with solid par-ticles having a bimodal distribution. The same choice was done by Jiang and Zhang [31] who analyzed the flow of a mixture of solid nitrogen particles and liquid nitrogen in a horizontal pipe.

Krampa-Morlu et al. [32] studied the effect of the solid phase boundary conditions on the head loss predictions for dense liquid–solid flows in a vertical pipe using a two-fluid model. The authors investigated the no-slip condition, the free-slip condition (i.e. zero wall shear stress),

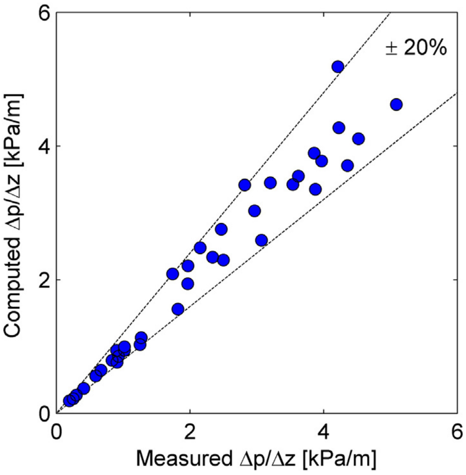

Fig. 2. Predictive capacity of the earlier version of our two-fluid model [6] with regard to the pressure gradient. Parity plot of computed versus measured values obtained by different experimenters [7,22,23].

two partial slip boundary conditions [33,34], and the wall shear stress formulation of Bartosik [12]. They concluded that the solid phase no-slip and free-slip boundary conditions are not appropriate for reproduc-ing the flow configurations studied in this work, investigated experi-mentally by Shook and Bartosik [35]. The partial slip and the shear stress formulations performed better, but could not reproduce the effect of the delivered solid volume fraction on the pressure gradient.

Recently, we made a similar investigation [36] and found that the application of the standard wall function of Launder and Spalding [29] for single-phase flows to both phases yields predictions of the pressure gradient with deviations of about ±20% with respect to most of the experimental data of Gillies et al. [7]. For this reason, we employed this boundary condition in our earlier two-fluid model [6] obtaining the results of Fig. 2. We also underlined that, even if capable in procuring fairly good estimation of the pressure gradient whatever the value of d_p^+ is, this boundary condition appears most reliable when the size of the particle is small compared to the extension of the log law region of the boundary layer, say for $d_p^+ < 50$. Anyway, we didn't perform an extensive analysis of the capacity of our model to correctly predict the pressure gradient of slurry flows in horizontal pipes as d_p^+ varies, and only briefly explored flows with large d_p^+.

In the present paper we present a new two-fluid model, which shows better performance than the earlier one as well as those available in the literature so far. The added value of this work resides in the following aspects. An original wall boundary condition for the solid phase makes the model capable in reproducing the effect of particle–wall interactions over a wide range of d_p^+. A better characterization of the viscosity of the mixture allows accounting for the effect of particle shape explicitly. These new features allowed enlarging the range of applicability of the model compared to the earlier one. At last, the use of a more efficient solution procedure helps in significantly lowering the computational burden.

The remainder of the paper is divided in two sections, followed by the conclusions. Section 2 illustrates the new two-fluid model, underlining the improvements made with respect to our previous one. Section 3 reports the validation of the model by comparison with exper-imental data from different experimenters [7,16,22,23,37,38].

2. Mathematical model

2.1. The new two-fluid model

As already mentioned, in the two-fluid models both phases are treated as interpenetrating continua. The reader is referred to our previous works [3,6] for a detailed discussion about the averaging processes leading to the equations of our model. The flows considered in this paper are assumed statistically steady, and the mass and momentum equations are as follows:

$$\nabla\cdot(\alpha_k\rho_k\mathbf{U}_k)-\nabla\cdot\left(\frac{\mu_{t,f}}{\sigma_\alpha}\nabla\alpha_k\right)=0 \tag{5}$$

$$\begin{aligned}\nabla\cdot(\alpha_k\rho_k\mathbf{U}_k\mathbf{U}_k) = {}&-\alpha_k\nabla P+\nabla\cdot\left[\alpha_k\left(T_k+T_{t,k}\right)\right]+\\ &+\alpha_k\rho_k\mathbf{g}+\mathbf{M}_k+\nabla\cdot\left(\frac{\mu_{t,f}}{\sigma_\alpha}\mathbf{U}_k\nabla\alpha_k\right)\end{aligned} \tag{6}$$

where the subscript k is a phase indicator parameter which is equal to f for the fluid and p for the particles. Moreover, α_k is the local average volume fraction, ρ_k is the density, $\mathbf{U}_k$ is the average velocity vector, σ_α is the turbulent Schmidt number for volume fraction, set equal to 0.7, P is the average pressure, T_k and $T_{t,k}$ are the viscous and turbulent stress tensors respectively, $\mathbf{g}$ is the gravitational acceleration vector, and $\mathbf{M}_k$ is the generalized drag per unit volume, which will be discussed later.

The viscous stress tensor and the turbulent stress tensor are given by:

$$T_k=2\mu_kD_k \qquad T_{t,k}=2\mu_{t,k}D_k \tag{7}$$

where μ_k is the dynamic viscosity, $\mu_{t,k}$ is the eddy viscosity, and D_k is the deformation tensor, given by:

$$D_k=\frac{1}{2}\left[\nabla\mathbf{U}_k+(\nabla\mathbf{U}_k)^+\right]. \tag{8}$$

The presence of the viscous stress term in the solid phase is a peculiar feature of the improved model, and allows procuring better prediction of the inter-granular stresses among the colliding particles. Following Enwald et al. [39], the viscosity of the solid phase μ_p is evaluated from that of the mixture μ_m (which will be discussed later) by assuming a linear relationship between μ_m and μ_f, μ_p, so that:

$$\mu_m=\rho_p\alpha_p+\mu_f\alpha_f. \tag{9}$$

The interfacial momentum transfer term $\mathbf{M}_k$, which accounts for the momentum transfer between the phases, is treated as analogous to the earlier version of the model. Since a literature review [19,40] and preliminary simulations revealed that lift, virtual mass and history forces are substantially negligible for the flows considered here, $\mathbf{M}_k$ reduces to the stationary drag, and is given by:

$$\mathbf{M}_f=-\mathbf{M}_p=\frac{3}{4d_p}C_d\alpha_p\rho_f|\mathbf{U}_p-\mathbf{U}_f|\left(\mathbf{U}_p-\mathbf{U}_f\right) \tag{10}$$

where C_d is the drag coefficient, evaluated by means of the Shiller and Naumann [41] formula:

$$C_d=\max\left[\frac{24}{\mathrm{Re}_p}\left(1+0.15\mathrm{Re}_p^{0.687}\right),0.44\right] \tag{11}$$

in which Re_p is the particle Reynolds number.

In order to account for the presence of other particles, the particle Reynolds number is expressed in term of the viscosity of the mixture instead of that of the fluid, and is therefore given by $\mathrm{Re}_p=\rho_f|\mathbf{U}_p-\mathbf{U}_f|d_p/\mu_m$. If coupled with an expression of μ_m which tends to infinity as the local average volume fraction α_p approaches the maximum packing value $\alpha_{\max}$, this definition of Re_p allows preventing the solids from overpacking without introducing a collisional pressure term in the dispersed-phase momentum equations, thereby contributing to the stability of the two-fluid model. In our earlier model we found that the formula of Mooney [42] for μ_m procured good agreement with the experimental evidence using a fixed set of empirical coefficients. How-ever, other materials than sand have been explored only briefly and ap-parently none of the sands considered in the validation tests had any peculiarity in the shape of the grains. The poorer performance of the model in case of sand grains of highly non-spherical grains [3] led us to think that the correlation for μ_m should be dependent on the charac-teristics of the solid particles in the slurry. The following exponential ex-pression, developed by Cheng and Law [43], is able to match well with many expression for μ_m available in the literature depending on the value of its only empirical coefficient β:

$$\mu_m = \mu_f \exp\left\{\frac{2.5}{\beta}\left[\frac{1}{\left(1-\alpha_p\right)^{\beta}-1}\right]\right\}. \tag{12}$$

Actually, according to Eq. 12, the viscosity of the mixture doesn't tend to infinity as the maximum packing volume fraction (which actually does not appear in the correlation) is approached. Nevertheless, the strongly increasing trend of μ_m with α_p allows avoiding particle interpenetration even if a particle collisional pressure term is absent in the momentum equation for the solid phase.

It is worth noticing that, due to the absence of an appropriate closure model, the effect of the hydrodynamic lift force is ignored. As confirmed by our numerical simulations, this may result in an overestimation of the predicted pressure gradient for the flow conditions involved in this effect.

The eddy viscosity of the fluid phase $\mu_{t,f}$ is evaluated by means of the following extension [44,45] of the standard high-Reynolds form of the $k-\varepsilon$ model of Launder and Spalding [46] to two-phase flows, apart from the inclusion of phase-diffusion terms, which are required for consistency with the corresponding terms in the phase continuity equations [45,47]:

$$\begin{aligned}\nabla\cdot\left(\alpha_f\rho_f\mathbf{U}_f k\right) &= \nabla\cdot\left[\alpha_f\left(\mu_f+\frac{\mu_{t,f}}{\sigma_k}\right)\nabla k\right]\\ &\quad+\alpha_f\rho_f(P_k-\varepsilon)+\nabla\cdot\left[\frac{\mu_{t,f}}{\sigma_\alpha}k\nabla\alpha_f\right]\end{aligned} \tag{13}$$

$$\begin{aligned}\nabla\cdot\left(\alpha_f\rho_f\mathbf{U}_f\varepsilon\right) &= \nabla\cdot\left[\alpha_f\left(\mu_f+\frac{\mu_{t,f}}{\sigma_\varepsilon}\right)\nabla\varepsilon\right]+\alpha_f\rho_f\frac{\varepsilon}{k}(C_{1\varepsilon}P_k-C_{2\varepsilon}\varepsilon)\\ &\quad+\nabla\cdot\left[\frac{\mu_{t,f}}{\sigma_\alpha}\varepsilon\nabla\alpha_f\right]\end{aligned} \tag{14}$$

$$\mu_{t,f} = \rho_f C_\mu\frac{k^2}{\varepsilon} \tag{15}$$

in which $P_k = 2\rho_f\mu_f D_f:\nabla\mathbf{U}_f$ is the volumetric production rate of k due to the working of the Reynolds stresses against the mean flow. The standard values [46] of the model constants are employed, namely $\sigma_k = 1.0$, $\sigma_\varepsilon = 1.314$, $C_\mu = 0.09$, $C_{1\varepsilon} = 1.44$, and $C_{2\varepsilon} = 1.92$.

The simple equality $\mu_{t,p} = \rho_p\mu_{t,f}/\rho_f$ proposed by Issa and Oliveira [48] for the evaluation of $\mu_{t,p}$ proved capable in procuring reliable prediction of the main features of the flow.

2.2. Computational domain and boundary conditions

The computational domain is shown in Fig. 3, where it is evident that flow and geometrical symmetry about the vertical axis has been exploited by solving only over one half of the pipe section. At the pipe inlet, we imposed the mass fluxes of the two phases, $\rho_f\alpha_f^{in}U_{z,f}^{in}$ and $\rho_p\alpha_p^{in}U_{z,p}^{in}$, the average axial velocities of the two phases, $U_{z,f}^{in}$ and $U_{p,f}^{in}$, the turbulent kinetic energy, k^{in}, and its dissipation rate, ε^{in}. The boundary-layer theory of Prandtl and Nikuradse [49] for fully-developed single-phase flow in a pipe was exploited to determine the distributions of $U_{z,f}^{in}$, $U_{z,p}^{in}$, k^{in}, and n^{in}. No slip is assumed between the phases at the inlet section, and therefore the same velocity distribution is applied to the fluid and the particles ($U_{z,f}^{in} = U_{z,p}^{in}$).

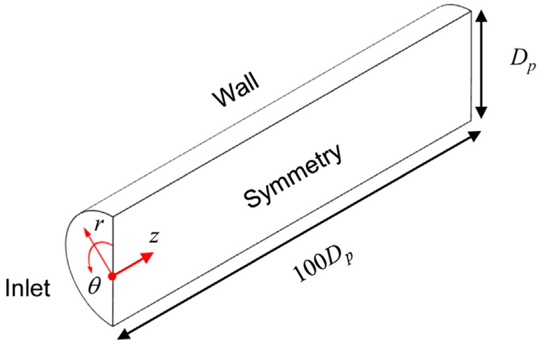

Fig. 3. Computational domain and boundary conditions.

$$\begin{aligned}
&U_{z,f}^{in} = U_{z,p}^{in} = V_s\frac{(N+1)(2N+1)}{2N^2}\quad\left.1-\frac{2r}{D_p}\right)^{1/N}\\
&N = \frac{1}{\sqrt{f}}\qquad f = \left[\frac{1}{1.82\log(\mathrm{Re}_b)-1.64}\right]^2\\
&k^{in} = V_s^2\frac{f}{8}\left[1+\frac{2}{3}\frac{2r}{D_p}+\frac{10}{3}\left(\frac{2r}{D_p}\right)^3\right]\\
&\varepsilon^{in} = C_\mu^{3/4}\frac{k^{3/2}}{l_m}\\
&l_m = \frac{D_p}{2}\left[0.14-0.08\frac{2r}{D_p}-0.06\left(\frac{2r}{D_p}\right)^4\right]
\end{aligned} \tag{16}$$

where Re_b is a bulk Reynolds number defined with respect to the pipe diameter D_p and the slurry superficial velocity V_s. The inlet volume frac-tions of both phases, α_f^{in} and α_p^{in}, are taken as uniformly distributed. No outlet condition is required since the algorithm of Patankar and Spalding [50] for parabolic flows is employed for the numerical solution of the equations (see subsection 2.4). A length of the computational do-main equal to $100D_p$ proved sufficient to ensure that fully-developed flow conditions are attained.

At the pipe wall, the equilibrium wall function of Launder and Spalding [29] for smooth walls is employed to evaluate the resultant fluid velocity parallel to the wall at the first grid node $\mathbf{U}_f^{//}$, the turbulent kinetic energy k_w, and its dissipation rate ε_w in the near-wall cells, sketched in Fig. 4.

$$\frac{\left|\mathbf{U}_f^{//}\right|}{u_f^*} = \frac{1}{\,}\ \ln\ \left.E\frac{\rho_f u_f^* y}{\mu_f}\right) \tag{17}$$

$$k_w = \frac{u_f^*}{\sqrt{C_\mu}} \tag{18}$$

$$\varepsilon_w = C_\mu^{3/4}\frac{k_w^{3/2}}{\kappa y} \tag{19}$$

In the above reported equations, $\kappa = 0.41$ is the von Karman constant, E is a roughness parameter which was set to 8.6 as appropriate for smooth walls, and y is the normal distance of the first grid point from the wall. For reasons which will be clarified later, it is convenient to rearrange Eq. 17 in terms of the fluid wall shear stress τ_w as follows:

$$\tau_{w,f} = \rho_f s_f|\mathbf{U}_f^{//}|\mathbf{U}_f^{//} \tag{20}$$

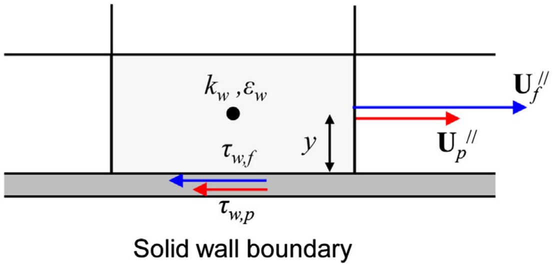

Fig. 4. Sketch of a near-wall cell.

where s_f is the friction factor of the fluid phase, given by the following implicit equation:

$$s_f = \left[\frac{\kappa}{\ln\left(E\mathrm{Re}_{w,f}\sqrt{s_f}\right)}\right]^2 \tag{21}$$

in which $\mathrm{Re}_{w,f} = \rho_f|\mathbf{U}_f^{//}|y/\mu_f$.

Due to its relevance, the wall boundary condition for the solid phase will be described in detail in a separate subsection.

2.3. New wall boundary condition for the solid phase

The new wall boundary condition for the solid phase was developed starting from the consideration that the standard wall function of Launder and Spalding [29] for the average particle velocity procures reliable prediction of the pressure gradient only if the particles are relatively small compared to the extension of the logarithmic portion of the boundary layer. Therefore, it is proposed to apply a particle wall shear stress which reduces to the standard wall function of Launder and Spalding [29] for low values of d_p^+ and to an expression similar to that of Ferre and Shook [9] (Eq. 3) for high values of d_p^+, as follows:

$$\tau_{w,p} = \rho_p s_p |\mathbf{U}_p^{//}|\mathbf{U}_p^{//} \tag{22}$$

where $\mathbf{U}_p^{//}$ is the resultant particle velocity parallel to the wall at the first grid node (Fig. 4). The friction factor of the solid phase, s_p, is calculated as:

$$s_p = \Lambda s_{p,1} + (1-\Lambda)s_{p,2} \tag{23}$$

where Λ is a ramp function ranging from 1 for $d_p^+ \le 30$ to 0 for $d_p^+ \ge 50$ and $s_{p,1}$ and $s_{p,2}$ are given by:

$$s_{p,1} = \left[\frac{\kappa}{\ln\left(E\mathrm{Re}_{w,p}\sqrt{s_{p,1}}\right)}\right]^2 \tag{24}$$

$$s_{p,2} = 0.3105\mathrm{Re}_{d,p}^{-0.25}\left(\frac{d_p}{l}\right)^{0.75}\left(\frac{\mu_m}{\mu_f}\right)^{0.3} \tag{25}$$

in which l is the turbulence length scale, assumed equal to one tenth of the pipe diameter, and $\mathrm{Re}_{w,p}$ and $\mathrm{Re}_{d,p}$ are the two local Reynolds numbers defined as:

$$\mathrm{Re}_{w,p} = \frac{\rho_p|\mathbf{U}_p^{//}|y}{\mu_p} \qquad \mathrm{Re}_{d,p} = \frac{\rho_p|\mathbf{U}_p^{//}|d_p}{\mu_f}. \tag{26}$$

From Eq. 23 it is evident that the proposed wall boundary condition for the solid phase is a combination of two sub-models by a weighted sum through the variable Λ depending on $d_p{}^+$. In particular, the former sub-model (Eq. 24) is the analog of the equilibrium wall function of Launder and Spalding [29] for the solid phase (Eq. 21). The latter sub-model (Eq. 25) is a local formulation of the bulk expression of Ferre and Shook [9] (Eq. 3), in which the superficial velocity of the slurry V_s and the linear volume fraction λ are replaced by $\mathbf{U}_p^{//}$ and μ_m/μ_f, respectively. The values of the numerical coefficients of Eq. 25 have been determined by matching the predictions of our two-fluid model with the pressure gradient data from [7,16,23,38], as discussed in the next section.

2.4. Computational methodology and consistency of the numerical solution

The general-purpose, commercial CFD code PHOENICS version 2011 was employed for the numerical solution of the finite-volume analog of the mathematical model described above. This is done by means of the built-in Eulerian, two-fluid, Inter-Phase Slip Algorithm (IPSA) of Spalding [44,51] together with user-defined functions and subroutines for implementation of specific constitutive equations and boundary conditions. Since straight pipe flows are parabolic according to the def-inition of Patankar and Spalding [50], the solution of the finite volume equations is performed by means of a specific calculation procedure which allows reducing considerably the CPU time. This procedure is de-scribed in [50] for single-phase flows. Its coupling with the two-phase IPSA is available in the PHOENICS code but has never been formally pub-lished, even if it has been well documented by Malin [52] for external flows. The basic idea of this procedure is to simplify the finite volume equations by dropping the downstream terms, and then employ a marching integration along the main flow direction indicated as z in Fig. 5. Solutions are obtained at planes of constant z, referred to as slabs, which are arrived by taking successive increments along the z direction. At each slab, the calculations are performed following the elliptic-staggered formulation in which the scalar variables are evaluated at the cell centers and the crosswise velocity components, $U_{\theta,k}$ and $U_{r,k}$, at the cell faces. The control volumes for the streamwise velocity, $U_{z,k}$, are not staggered. Central differencing is employed for the diffusion terms, while the convection terms are discretized using the hybrid differencing scheme of Spalding [53]. The solution procedure assumes the uncoupling of longitudinal and lateral pressure gradients. The first, regarded as uniform over a cross-section, is the outcome of the integral mass-conservation equation. The latters are obtained from the local continuity equation as in the original IPSA [44,45]. The numerical solution procedure requires appropriate relaxation of the field variables to achieve convergence. Inertial relaxation is applied to the momentum equations with a false-time step of 0.01 s, which is the order of the cell convection time. A linear relaxation factor of 0.4 is applied to all other flow variables.

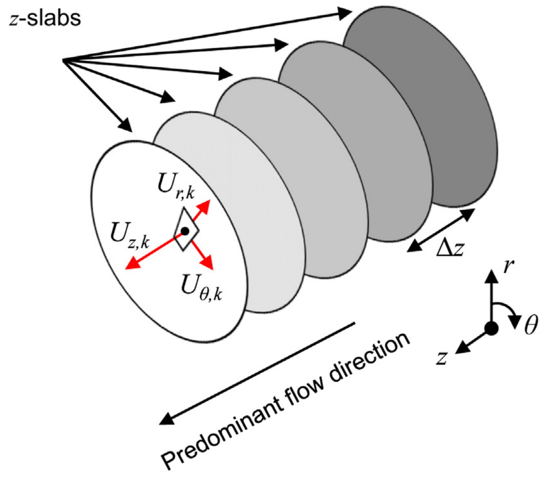

Fig. 5. Sketch of the solution procedure.

A polar structured mesh consisting of 540 cells (15 angular by 36 radial) was used to discretize each slab. A grid independence study revealed that such number of slab cells is sufficient to provide a consistent numerical solution. However, as in our earlier work [6] the predicted pressure gradient was found dependent upon the distribution of the cells and, particularly, upon the wall distance of the first grid nodes. Therefore, the mesh was designed in such a way that $y^+ = \rho_f\, u_f^* y/\mu_f \approx 30$ for the first grid nodes, as this is the smallest possible value consistent with the application of Eq. 17. At last, a forward step size Δz (Fig. 5) equal to one tenth of the pipe diameter proved sufficient to procure grid-independent predictions.

The PHOENICS solver was run until the sum of the absolute residual errors over each slab is less than 1% of reference quantities based on the total inflow of the variable in question. This is typically achieved in about 20 iterations per slabs. The use of the marching procedure de-scribed above allows achieving a converged solution in about 60 s CPU time with a quad-core Intel processor with 2.83 GHz and 8 GB RAM, much lower than the 1600 s CPU time required by the original IPSA algorithm.

3. Results and discussion

The two-fluid model presented here has been validated against several experimental data collected by different experimenters and reported in the literature [7,16,22,23,37,38]. In line with the applications addressed in this research, the focus is on slurries in which the solid phase consists of sand particles, but the case of spherical glass beads has also been briefly explored to better establish the applicability of the model. Moreover, since one of the key features of this work is the new wall boundary condition for the solid phase (strictly connected with the mechanical contribution to friction), the predictive capacity of the model has been checked mostly with regard to the pressure gradient, which is dedicated the majority of this paper. The two other parameters of most engineering interest, which are the particle distribution and the velocity distribution, are considered at the end of this section.

As already reported in the “Introduction”, this work concerns fully-suspended flows, which occur when the superficial velocity of the slurry V_s exceeds the threshold value at which transition to moving bed flow occurs, V_D. We were able to verify this condition only for few cases in the dataset considered for the validation [7,16,22,23,37,38]. Therefore, unless specific information were available we considered only the data referring to flows in which $V_s > 1.5 V_{D,\mathrm{Wasp}}$, where $V_{D,\mathrm{Wasp}}$ is the es-timated deposition velocity according to the formula of Wasp [2] (Eq. 1). The 1.5 factor allowed assuming with reasonable safety the absence of particle accumulation.

Since the proposed wall boundary condition for the solid phase is a combination of two sub-models which apply for different ranges of d_p^+ (via the ramp function Λ in Eq. 23), we decided to validate each sub-model separately. At first we focused on flows in which $\Lambda = 1$ in the near wall-cells, so that the wall-function sub-model (Eq. 24) applies.

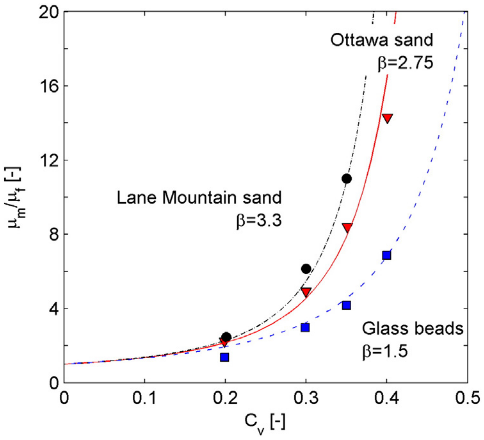

Fig. 6. Relative viscosity as a function of the solid volumetric concentration in the viscom-eter for Ottawa sand, Lane Mountain sand, and glass beads. (Markers = experimental measurements of Shaan et al. [22]; lines = best-fit estimates by Eq. 12).

The experiments of Shaan et al. [22], Gillies et al. [7], and Matousek [23], referred to as C1 to C5 in Table 1, were employed for testing the predictive capacity of the two-fluid model.

Cases C1 and C2 are particularly significant as they allow establishing the capability of the two-fluid model in reproducing the effect of grain shape. The sands considered in these tests, characterized by nearly equal density and size, differ significantly with respect to the shape of the grains, which is particularly irregular in the Lane Mountain sand. The improved two-fluid model can account for the effect of grain shape by means of the law linking the viscosity of the mixture μ_m to the solid volume fraction α_p (Eq. 12) and, particularly, via the empirical coefficient β. Shaan et al. [22] used a concentric viscometer to measure the viscosity of the slurries tested in the loop. By replacing the local solid volume fraction α_p with the solid volumetric concentration in the vis-cometer C_v, we determined the best-fit values of β, which were 2.75 and 3.3 for Ottawa sand and Lane Mountain sand respectively (Fig. 6). These values were used in the simulations of the flow conditions referred to as C1 and C2 in Table 1.

Fig. 7(a) and (b) reports the results for the two kinds of sand, comparing the predicted pressure gradient – depicted as a function of the slurry superficial velocity – with the experimental data of Shaan et al. [22], which have been connected by straight line segments for the sake of clarity. The very good agreement between predictions and mea-surements (the deviations being generally lower than 5%, as indicated in the parity plot depicted in Fig. 8a) proves the reliability of our two-fluid model when $d_p^+ \leq 30$ and therefore the “wall-function” sub-model ap-plies to the solid phase. Anyway, the case of $C = 40\,\%$ was not consid-ered for the Lane Mountain sand since it is characterized by anomalous low values of pressure gradient which Shaan et al. [22] at-tributed to the transition to the laminar flow regime. Our model applies to turbulent flows only, and proved incapable in reproducing these

Table 1
Flow conditions considered in the validation study.

Case ID	Experimenter	D_p [mm]	Particles	ρ_p[kg/m^3]	d_p[μm]	C [%]	V_s[m/s]
C1	Shaan et al. [22]	53.2	Ottawa sand	2660	85	15 ÷ 40	3 ÷ 5
C2	Shaan et al. [22]	53.2	Lane Mountain sand	2655	90	15 ÷ 35	3 ÷ 5
C3	Shaan et al. [22]	53.2	Glass beads	2440	100	15 ÷ 45	3 ÷ 5
C4	Gillies et al. [7]	102.7	Sand	2650	90	19 ÷ 32.5	3 ÷ 7
C5	Matousek [23]	155.0	Sand	2650	120	26	3.2 ÷ 4
C6	Gillies et al. [7]	102.7	Sand	2650	280	11 ÷ 40	≈ 3 ÷ 7
C7	Matousek [23]	155.0	Sand	2650	370	26	3.75 ÷ 9
C8	Lee et al. [38]	155.0	Sand	2650	540	7 ÷ 22	≈ 3.5 ÷ 7.5
C9	Lee et al. [38]	204.0	Sand	2650	540	7 ÷ 26	≈ 4 ÷ 5.5
C10	Shaan and Shook [16]	104.7	Sand	2650	640	20 ÷ 30	≈ 3.5 ÷ 5.5
C11	Roco and Shook [37]	50.7	Sand	2650	510	≈11	3.2 ÷ 4

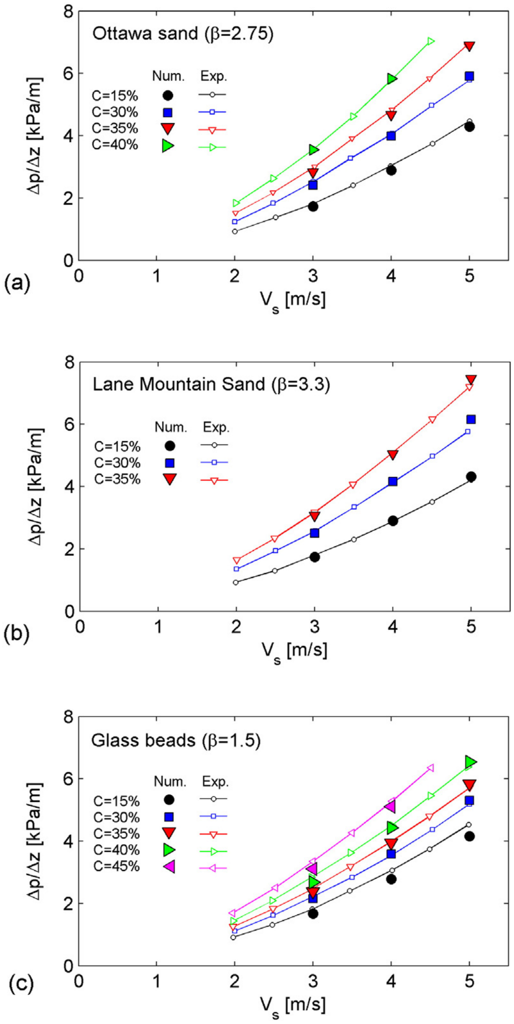

Fig. 7. Pressure gradient versus slurry velocity for different flow conditions in which $\Lambda = 1$ in Eq. 23: comparison between our CFD predictions (solid symbols) and the experimental data of Shaan et al. [22] (open symbols), connected by straight line segments.

experiments. Case C3 in Table 1, whose results are depicted in Fig. 7(c), extends the validation of the model to slurries in which the solid phase consists of spherical glass beads, provided that the mixture viscosity correlation is properly defined. Here we employed a value of β equal to 1.5, which procures the best agreement with the mixture viscosity measurements of Shaan et al. [22] reported in Fig. 6.

The main drawback of this approach is that the mixture viscosity correlation can be rarely determined accurately, because experimental measurements of the mixture viscosity are available in very few cases. Since this may become an issue in the engineering applications, our in-dication is to set $\beta = 3$ for sand–water slurries unless mixture viscosity data allow a more precise characterization of the solid phase. The use of such value of β instead of those obtained from the mixture viscosity data depicted in Fig. 6 results in a worsening of about few percents in the pressure gradient predictions for cases C1 and C2, but only for the highest values of delivered solid volume fraction where the influence of *ta* on μ_m is greater. The same value of β was used when reproducing the experiments of Gillies et al. [7] and Matousek [23] (cases C4 and C5 in Table 1), who didn't report measurements of the mixture viscosity. It is observed that, even in the lack of a more precise characterization of this parameter, assuming $\beta = 3$ results in deviations between computa-tions and experiments not greater than about 10% (Fig. 8(b)), with considerable improvement compared to our earlier model (Fig. 2).

The validation is now addressed at flows in which $\Lambda < 1$ and therefore the Bagnold sub-model (Eq. 25) applies, possibly in conjunction

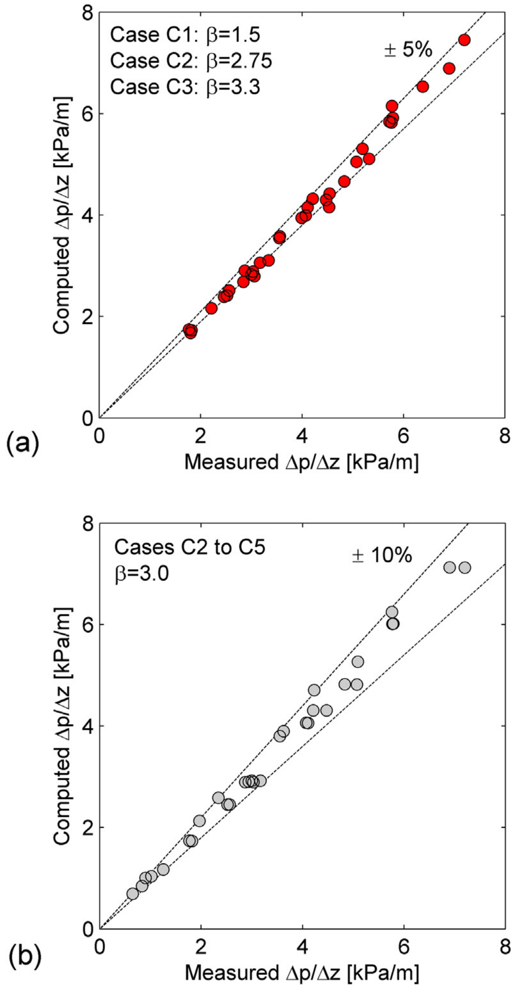

Fig. 8. Parity plot “computed pressure gradient” versus “measured pressure gradient” for:(a) cases C1 to C3 [22] in Table 1, with the value of β in Eq. 12 obtained from the mixture viscosity data depicted in Fig. 6; (b) cases C2 to C5 [7,22,23] in Table 1 with $\beta = 3.0$ in Eq. 12.

with the wall-function one. Basically, these flows occur when coarse particles flow at high velocity. The high pumping capacity required by these flows may contribute to explain the scarcity of experimental data available in the literature. The tests referred to as C6 to C10 in Table 1 were performed in four different test rigs, namely a 103-mm and a 105-mm test rig at the Saskatchwan research council, Saskatoon, CA-SK (cases C6 and C10 respectively), a 155-mm pipe rig at the Delft University of Technology, Delft, NL (cases C7 and C8), and a 204-mm pipe rig at the Hyundai Institute of Construction Technology, Yongin-City, KR (case C9). Since the deposition velocity was not declared by the experimenters, we considered only the data fulfilling the already-mentioned criterion $V_s > 1.5V_{D,\mathrm{Wasp}}$ in order to guarantee the complete suspension of the particles. Moreover, we set $\beta = 3$ in Eq. 12 as no indi-cation is given regarding the viscosity of the mixture. Based on the above-mentioned references we reproduced numerically more than 40 different flow conditions, which allowed us determining a set of numerical coefficients in Eq. 25 to obtain good agreement between computations and measurements.

As an example, Fig. 9 shows the pressure gradient versus velocity plots for the validations tests C6 to C8, and proved the reliability of the solid wall boundary condition in reproducing the mechanical contribu-tion to friction also when $d_p^+ > 30$. In the former case, an overestimation up to about 25% occurs for the highest values of *C* and V_s. These deviations are worthy of investigations in future works. A possible preliminary explanation is that the two-fluid model doesn't account for the

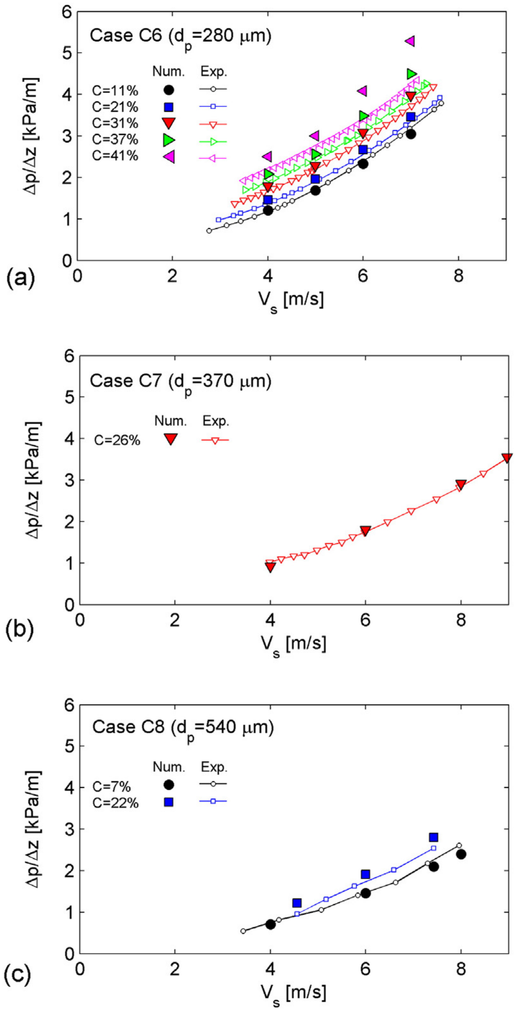

Fig. 9. Pressure gradient versus slurry velocity for different flow conditions in which $\Lambda <$ 1 in Eq. **23**: comparison between our CFD predictions (solid symbols) and the experimental data of Gillies et al. [7], Matousek [23], and Lee et al. [38] (open symbols), connected by straight line segments.

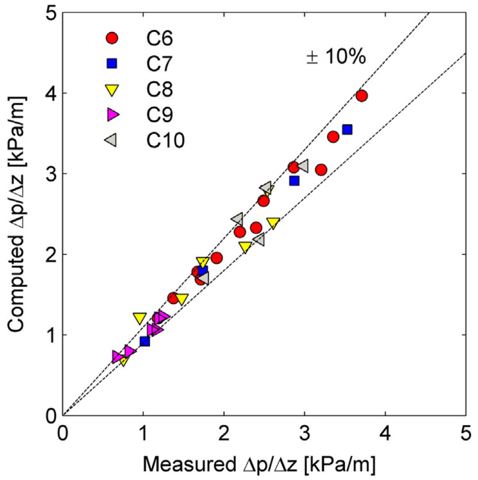

Fig. 10. Parity plot “computed pressure gradient” versus “measured pressure gradient” for cases C6 to C10 in Table 1 [7,16,23,28].

effect of the hydrodynamic lift force which, according to the experimenters themselves [7], is very significant for these flows. Unfortunately, the C6 series appear to be the only experimental data available in the literature referring to flows with $\Lambda < 1$ and $C > 30\,\%$. For these reason, we restrict the validity of Eq. 25 to the following flow conditions: pipe diameter from 100 to 200 mm, particle size from 280 to 640 μm, solid volume fraction from 7 to 30%, and slurry velocity up to 9 m/s. Focusing on the tests falling in this range of variability, the deviations between computations and experiments were generally not greater than about 10% (Fig. 10), around half of that of the earlier model (Fig. 2).

As previously anticipated, at the end of this section we will investigate the predictive capacity of the two-fluid model in terms of other parameters of engineering interest, such as particle distribution and velocity distribution. As for the pressure gradient, the analysis will be performed for the two cases $\Lambda = 1$ and $\Lambda < 1$ (actually $\Lambda = 0$), in order to test each of the two sub-models for s_p. As far as the particle distribution is concerned, reference is made to the flow conditions C4, C6, and C7 in Table 1, investigated experimentally by Gillies et al. [7] and Matousek [23]. Consistently with the fact that the experimenters used the γ-ray absorption method for performing their measurements, the particle distribution was quantified by means of the chord-average volume fraction profile. The results, shown in Fig. 11, revealed the capability of the model in estimating this feature of the flow about as accurately as the earlier one. Particle velocity data from case C4, referring to flows where $d_p^+ < 30$ and therefore $\Lambda = 1$ have been employed for validating the model also with respect to the velocity distribution, while the case of $\Lambda = 0$ has been tested with respect to the experiments of

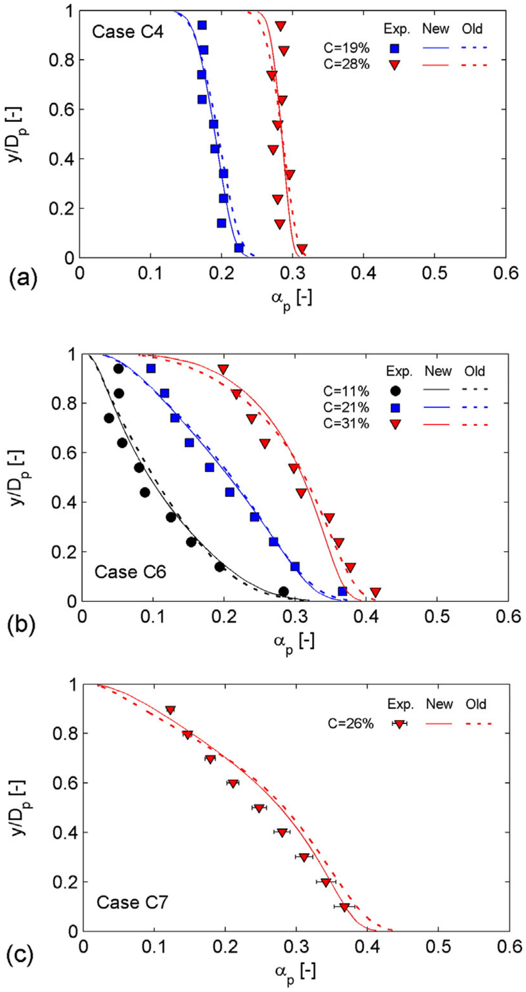

Fig. 11. Chord-average solid volume fraction distribution for the following flow conditions: (a) test case C4 with $V_s = 3$ m/s; (b) test case C6 with $V_s = 5.4$ m/s; (c) test case C7 with $V_s = 6$ m/s. Comparison between the experiments of Gillies et al. [7] and Matousek [23] (which have error bars corresponding to the uncertainty declared by the author), the predictions of our earlier model [6] and those of the current one.

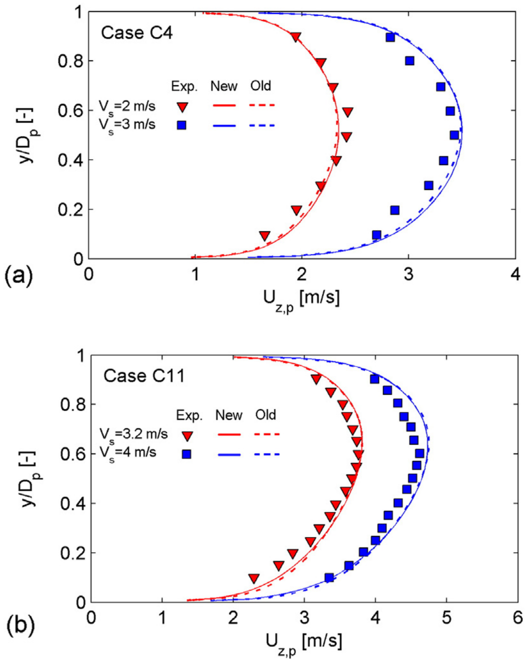

Fig. 12. Mixture velocity profile along the vertical diameter for the following flow conditions: (a) test case C4 with $V_s = 2$ m/s and $V_s = 3$ m/s; (b) test case C11 with $V_s = 3.2$ m/s and $V_s = 4$ m/s. Comparison between the experiments of Gillies et al. [7] and Roco and Shook [37], the predictions of our earlier model [6] and those of the current one.

Roco and Shook [37], who measured the particle velocity for the flow conditions referred to as C11 in Table 1.The modifications apported to the model produce no significant variation on the predictions of this parameter, which agree with the experiments for all the validation tests (Fig. 12). In particular, the two-fluid model preserves its capability of reproducing the shift of the maximum velocity towards the ceiling of the pipe, interpreted by many authors as the consequence of the slurry density gradient arising from the effect of gravity.

4. Conclusion

This study significantly improved the two-fluid model that we presented in an earlier paper [6] for the simulation of fully-suspended slur-ry flows in horizontal pipes. The main novelty resides in the wall boundary condition for the solid phase, obtained by combining two sub-models. If the particles are small compared to the boundary layer thickness, it reduces to the standard wall function of Launder and Spalding [29] and, otherwise, it reduces to an expression developed starting from the correlation of Ferre and Shook [9] for the Bagnold stresses. The numerical coefficients of this expression have been obtain-ed by matching the CFD predictions with pressure gradient measure-ments over this range of flow conditions: pipe diameter from 100 to 200 mm, sand particles of size from 280 to 640 μm, solid volume fraction from 7 to 30%, and slurry velocity up to 9 m/s. Other improvements in the constitutive equations for the solid phase and the interphase friction allowed accounting explicitly for the effect of particle shape. At last, a different solution algorithm allowed reducing significantly the CPU time, already low compared to similar models available in the literature. Extensive validation has been performed with respect to experimen-tal data available in the literature [7,16,22,23,37,38]. The new model proved capable in providing pressure gradient estimations within about ± 10 % of the measured value (Figs. 8(b) and 10) which can be reduced further if lab tests are performed for better characterizing the vis-cosity of the slurry (Fig. 8(a)). The effect of the hydrodynamic lift force is not accounted for due to the absence of a model for this force suitable for inclusion in a CFD code, and therefore the pressure gradient is likely to be overestimated when this effect plays an important role (Fig. 9(a)). However, the accuracy of the improved model is considerably higher compared to its earlier version [6] (Fig. 2) and its range of applicability wider. Moreover, the modifications do not affect the model's capability in reproducing the other features of these flows of most engineering in-terest, such as particle distribution (Fig. 11) and velocity distribution (Fig. 12). The wide applicability, the reliability of the predictions, and the computational efficiency make this model attractive for the engineering applications.

References

[1] P. Doron, D. Barnea, Flow pattern maps for solid–liquid flow in pipes, Int. J. Multiphase Flow 22 (2) (1996) 273–283.
[2] E.J. Wasp, J.P. Kenny, R.L. Gandhi, Solid Liquid Flow Slurry Pipeline Transportation, Publication, Clausthal, Germany, Trans. Tech, 1977.
[3] G.V. Messa, Two-fluid Model for Solid–Liquid Flows in Pipeline Systems, PhD Thesis, Politecnico di Milano University, Milano, Italy, 2013. Available at https:// www. politesi.polimi.it/handle/10589/74528.
[4] B.E.A. Jacobs, Design of Slurry Transport Systems, Elsevier Applied Science, London and New York, 2005.
[5] V. Matousek, Research developments in pipeline transport of settling slurries, Powder Technol. 156 (1) (2005) 43–51.
[6] G.V. Messa, M. Malin, S. Malavasi, Numerical prediction of fully-suspended slurry flow in horizontal pipes, Powder Technol. 256 (2014) 61–70.
[7] R.G Gillies, C.A. Shook, J. Xu, Modelling Heterogeneous Slurry Flow at High Velocities, Can. J. Chem. Eng. 82(5) (2004) 1060–1065.
[8] K.C. Wilson, R.S. Sanders, R.G. Gillies, C.A. Shook, Verification of the near-wall model for slurry flow, Powder Technol. 197 (3) (2010) 247–253.
[9] A.L. Ferre, C.A. Shook, Coarse particle wall friction in vertical slurry flows, Particul. Sci. Technol. 16 (1998) 125–133.
[10] R.G. Gillies, C.A. Shook, Modeling high concentration settling slurry flows, Can. J. Chem. Eng. 78 (2000) 709–716.
[11] V. Matousek, Non-stratified flow of sand–water slurries, in: N. Heywood (Ed.), Proc. 15th Int. Conf. on Hydrotransport, BHRG, Banff, Canada, 2002 (3–5 June), pp. 563–574.
[12] A. Bartosik, Influence of coarse-dispersive solid phase on the “particle-wall” shear stress in turbulent slurry flow with high solid concentration, Arch. Mech. Eng. LVII(1) (2010) 45–68.
[13] C.A. Shook, S.M. Daniel, J.A. Scott, J.P. Holgate, Flow of suspensions in pipelines. Part 2: two mechanisms of particle suspension, Can. J. Chem. Eng. 46 (4) (1968) 238–244.
[14] M.R. Carstens, G.R. Addie, A sand–water slurry experiment, J. Hydr. Div. ASCE 107 (1981) 501–507.
[15] D.R. Kaushal, Y. Tomita, Experimental investigation for near-wall lift of coarser particles in slurry pipeline using γ-ray densitometer, Powder Technol. 172 (2007) 177–187.
[16] J. Shaan, C.A. Shook, Anomalous friction in slurry flows, Can. J. Chem. Eng. 78 (4) (2000) 726–730.
[17] K.C. Wilson, A. Sellgren, Interaction of particles and near-wall lift in slurry pipelines,
J. Hydraul. Eng. 129 (1) (2003) 73–76.
[18] L. Chen, Y. Duan, W. Pu, C. Zhao, CFD simulation of coal–water slurry flowing in horizontal pipelines, Korean J. Chem. Eng. 26 (4) (2009) 1144–1154.
[19] K. Ekambara, R.S. Sanders, K. Nandakumar, J.H. Masliyah, Hydrodynamic simulation of horizontal slurry pipeline flow using ANSYS-CFX, Ind. Eng. Chem. Res. 48 (17)(2009) 8159–8171.
[20] S.K. Lahiri, K.C. Ghanta, Slurry flow modeling by CFD, CI&CEQ 16 (4) (2010) 295–308.
[21] D.R. Kaushal, T. Thinglas, Y. Tomita, S. Juchii, H. Tsukamoto, CFD modeling for pipeline flow of fine particles at high concentration, Int. J. Multiphase Flow 43 (2012) 85–100.
[22] J. Shaan, R.J. Sumner, R.G. Gillies, C.A. Shook, The effect of particle shape on pipeline friction for Newtonian slurries of fine particles, Can. J. Chem. Eng. 78 (4) (2000) 717–725.
[23] V. Matousek, Pressure drop and flow patterns in sand-mixture pipes, Exp. Therm. Fluid Sci. 26 (6–7) (2002) 693–702.
[24] G.V. Messa, S. Malavasi, Computational investigation of liquid–solid slurry flow through an expansion in a rectangular duct, J. Hydrol. Hydromech 62 (3) (2014) 234–240.
[25] G.V. Messa, S. Malavasi, Numerical prediction of particle distribution of solid–liquid slurries in straight pipes and bends, Eng. Appl. Comput. Fluid Mech. 8 (3) (2014) 356–372.
[26] S. Malavasi, G.V. Messa, G. Ferrarese, Solid–liquid flows through a wellhead choke valve, Proc. ASME 2013 Pressure Vessels & Piping Division Conference PVP2013, Paris, France, 2013.
[27] A.P. Davis, E.E. Michaelides, Z.G. Feng, Particle velocity near vertical boundaries. A source of uncertainty in two-fluid models, Powder Technol. 220 (2012) 15–23.
[28] Z.G. Feng, M.E.C. Ponton, E.E. Michaelides, S. Mao, Using the direct numerical simu-lation to compute the slip boundary condition of the solid phase in two-fluid model simulations, Powder Technol. (2014), in press.
[29] B.E. Launder, D.B. Spalding, Mathematical Models of Turbulence, Academic Press, London, 1974.

[30] P.C. Johnson, R. Jackson, Frictional–collisional constitutive relations for granular materials, with application to plane shearing, J. Fluid Mech. 176 (1987) 67–93.

[31] Y.Y. Jiang, P. Zhang, Pressure drop and flow pattern of slush nitrogen in a horizontal pipe, AIChE J. 59 (5) (2013) 1762–1773.

[32] F.N. Krampa-Morlu, J.D. Bugg, D.J. Bergstrom, R.S. Sanders, J. Shaan, Frictional pressure drop calculation for liquid–solid vertical flows using two-fluid model. Proc 14th Annual Conference of the Computational Fluid Dynamics Society of Canada, Kingston, Canada, 2006.

[33] J. Ding, D. Gidaspow, A bubbling fluidization model using kinetic theory of granular flow, AIChE J. 36 (1990) 523–538.

[34] J. Ding, R.W. Lyczkowski, Three-dimensional kinetic theory modelling of hydrodynamics and erosion in fluidized beds, Powder Technol. 73 (1992) 127–138.

[35] C.A. Shook, A.S. Bartosik, Particle-wall stresses in vertical slurry flows, Powder Technol. 81 (2) (1994) 117–124.

[36] G.V. Messa, M. Malin, S. Malavasi, Numerical prediction of pressure gradient of slur-ry flows in horizontal pipes, Proc. ASME Pressure Vessels & Piping Division Confer-ence PVP2013, France, Paris, 2013. 2013.

[37] M.C. Roco, C.A. Shook, Modeling of slurry flow: the effect of particle size, Can. J. Chem. Eng. 61 (1983) 494–503.

[38] M.S. Lee, V. Matousek, C.K. Chung, Y.N. Lee, Pipe size effect on hydraulic transport of Jumoonjin sand: experiments in a dredging test loop, Terra et Aqua 99 (2005) 3–10.

[39] H. Enwald, E. Peirano, A.E. Almstedt, Eulerian two-phase flow theory applied to fluidization, Int. J. Multiphase Flow 22 (1996) 21–66.

[40] J.N. Chung, T.R. Troutt, Simulation of particle dispersion in an axisymmetric jet, J. Fluid Mech. 186 (1) (1988) 199–222.

[41] L. Shiller, A. Naumann, A drag coefficient correlation, Z. Ver. Dtsch. Ing. 77 (1935) 318–320.

[42] M. Mooney, The viscosity of a concentrated suspension of spherical particles, J. Colloid Sci. 6 (2) (1951) 162–170.

[43] N.S. Cheng, A.W.K. Law, Exponential formula for computing effective viscosity, Powder Technol. 129 (1–3) (2003) 156–160.

[44] D.B. Spalding, Numerical computation of multi-phase fluid flow and heat transfer, in: C. Taylor, K. Morgan (Eds.), Recent Advances in Numerical Methods in Fluids, Pineridge Press Limited, Swansea, UK, 1980, pp. 139–168.

[45] D.B. Spalding, PHOENICS: A General-Purpose Computer Program for Multi-Dimensional One- and Two-Phase Flow, CFDU Report HTS/81/11, Imperial College, London, 1981.

[46] B.E. Launder, D.B. Spalding, The numerical computation of turbulent flows, Comput. Meth. Appl. Mech. Eng. 3 (1974) 269–289.

[47] D.B. Spalding, Mathematical Modelling of Fluid-Mechanics, Heat-Transfer and Chemical-Reaction Processes: A Lecture Course, CFDU Report HTS/80/1, Imperial College, London, 1980.

[48] R.I. Issa, P.J. Oliveira, Assessment of a particle–turbulence interaction model in conjunction with an Eulerian two-phase flow formulation, Proc 2nd Int Symp. on Turbulence Heat and Mass Transfer1997. pp. 759–770.

[49] H. Schlichting, Boundary Layer Theory, McGraw-Hill, New York, 1960.

[50] S.V. Patankar, D.B. Spalding, A calculation procedure for heat, mass and momentum transfer in three-dimensional parabolic flows, Int. J. Mass Transfer 15 (1972) 1787–1806.

[51] D.B. Spalding, IPSA 1981: New Developments and Computed Results, CFDU Report HTS/81/2, Imperial College, London, 1981.

[52] M.R. Malin, Turbulence modelling for fluid flow and heat transfer in jets, wakes, and plumes, PhD Thesis, Imperial College, London, 1986.

[53] D.B. Spalding, A novel finite-difference formulation for differential expressions involving both first and second derivatives, Int. J. Numer. Methods Eng. 4 (4) (1972) 551–559.